Journal of
Materials Chemistry B

Materials for biology and medicine

Accepted Manuscript

This article can be cited before page numbers have been issued, to do this please use: S. Shukla, S. S. Sahoo, S. Kadian, M. Morgan and R. Narayan, *J. Mater. Chem. B*, 2026, DOI: 10.1039/D6TB00732E.

ROYAL SOCIETY OF CHEMISTRY

rsc.li/materials-b

View Article Online
DOI: 10.1039/D6TB00732E

MOF-based tri electrode aptasensor platform for effective detection of sepsis markers with minimal cross-interference

Shubhangi Shukla,[a] Siba Sundar Sahoo,[b] Sachin Kadian,[a] Meagan Morgan,[a] and Roger J. Narayan[a b]

[a]Joint Department of Biomedical Engineering, University of North Carolina and North Carolina State University, Raleigh, NC 27695, USA.

[b]Department of Materials Science and Engineering, North Carolina State University, Raleigh, NC 27695, USA

E-mail: rjnaraya@ncsu.edu

In recent years, several multiplexed point-of-care platforms have been developed as diagnostic tools for sepsis. However, the current versions suffer from poor electrode consistency, analyte interference, and complicated production challenges. Here, we report a polymethyl methacrylate (PMMA)-based trimodal multiplex sensor for the concurrent detection of three sepsis biomarkers: procalcitonin (PCT), C-reactive protein (CRP), and interleukin-6 (IL-6). The device has three active sensing areas. Each area contains a conductive paste comprising trypan blue (TB)-functionalized metal-organic framework (MOF). The MOF paste acts as a transduction layer and is modified with aptamers specific to each analyte. The design includes barriers, optimized channel geometries, and capillary stops to keep electrolytes separate, preventing cross-contamination and off-target binding. The TB-MOF material, with its extended π-conjugation, allows direct electron transfer, which is amplified by surface modification with 3-phosphonopropionic acid (3-PPA). This enhanced electron transfer reduces charge transfer resistance (Rct), lowers redox potential, and increases peak currents by ~ 5-10-fold compared to the unmodified MOF paste. The increased density and orientation of aptamers, caused by the phosphonic acid groups of 3-PPA, also increase the number of binding sites, leading to significant changes in electrochemical reversibility following immobilization. With such arrangements, the subsequent aptasensors achieved detection limits of approximately 0.204 pg mL^{-1} (PCT), 0.02 mg mL^{-1} (CRP), and 0.315 pg mL^{-1} (IL-6), with cross-reactivity below 5%. Overall, this single-formulation platform is graphene-free, shows reproducible baseline stability, and provides a cost-effective approach for producing disposable diagnostic cartridges for sepsis with high specificity.

Keywords: multiplexed biosensor, PMMA, aptamers, PCT, IL-6, CRP, MOF paste

View Article Online
DOI: 10.1039/D6TB00732E

1. Introduction

Sepsis is a medical condition associated with a dysregulated host response to infection and represents one of the major challenges in global healthcare. Patient outcomes depend critically on the speed and accuracy of diagnosis. The progression from early sepsis to septic shock necessitates rapid detection and patient stratification using key biomarker profiles, including procalcitonin (PCT), C-reactive protein (CRP), and interleukin-6 (IL-6).[1,2] Traditional assays such as ELISA and immunoassay-based methods are largely confined to central laboratory settings and require substantial infrastructure. These techniques often lack multiplexed detection capability and result in prolonged turnaround times. To address these limitations, point-of-care (POC) platforms are needed for multiplexed biomarker testing, enabling timely and personalized diagnosis.[2,3]

The quantities of these biomarkers vary considerably during the onset and progression of sepsis. As reported in the literature, PCT levels of 0.25–0.5 ng mL^{-1} are associated with local bacterial infection. A value of 1 ng mL^{-1} indicates systemic infection, while levels exceeding 10 ng mL^{-1} and up to 100 ng mL^{-1} reflect the onset of sepsis. The PCT levels rise within approximately 4 h of infection onset and peak at 8–24 h.[4,5] CRP is an acute-phase protein that is produced in response to infection or tissue injury. CRP levels begin to rise approximately 10–12 hours following sepsis onset. Levels above 10 μg mL^{-1} indicate sepsis.[6–7] Likewise, under normal physiological conditions, IL-6 reference levels range from 5 to 25 pg mL^{-1} and can reach up to 1000 pg mL^{-1} during sepsis. Blood IL-6 levels are strongly associated with sepsis prognosis, as high levels (500 pg mL^{-1}) are associated with increased mortality risk. Collectively, these dynamic biomarker profiles underscore their clinical utility in the early diagnosis and management of sepsis.[8–10]

Electrochemical sensors have gained considerable attention as analytical detection platforms. They offer high sensitivity, portability, and compatibility with low-cost fabrication. Recent studies have reported multiplexed devices capable of monitoring sepsis biomarkers, such as magneto-immunosensors for simultaneous PCT and CRP detection and graphene-nanocomposite-coated planar gold electrode-based multiplex platforms for detection directly in undiluted serum and other clinical samples.[11–13] These platforms demonstrated multi-biomarker detection in blood, incorporating advanced antifouling and low-noise surface designs. They have also demonstrated clinical feasibility through reduced assay times, which were enabled by microfluidic integration. However, most of these multiplexed platforms suffer from limitations such as inter-channel variability, analyte crosstalk, baseline drift, fabrication complexity, and inconsistent electrode geometries. Furthermore, reliance on graphene or other complex nanostructured materials poses reproducibility and scale-up challenges. Collectively, these limitations hinder the practical deployment of multiplexed electrochemical systems.

MOFs are large surface area, high-porosity coordination polymers, which have been extensively investigated for electrochemical applications.[14–16] Despite their unique structural properties, their application in biosensing remains limited, primarily due to insufficient intrinsic conductivity. Numerous efforts have been directed towards synthesizing electrically conductive MOFs, but most

View Article Online
DOI: 10.1039/D6TB00732E

reported systems exhibit poor electrical conductivity to fully exploit their biosensing potential. Prominent exceptions include MOFs derived from conjugated organic linkers such as tetrathiafulvalene (TTF), trypan blue (TB), and porphyrin derivatives, which exhibit sufficient conductivity. [14–16] To date, MOFs are primarily employed as solvent-dispersed thin films onto glassy carbon or screen-printed electrodes for biosensor fabrication. These films are further modified with biorecognition elements such as aptamers, enzymes, and antibodies, but often suffer from limited long-term stability and compromised sensing performance.

In this context, utilizing a carbon-free conductive MOF in paste form offers several notable advantages over conventional thin films. The paste architecture enables efficient electron transfer through percolation pathways, ensures mechanical stability, and prevents film delamination.[14] It also allows higher MOF loading, which facilitates a greater number of accessible active sites, and supports homogeneous chemical functionalization (e.g., 3-phosphonopropionic acid (3-PPA) treatment for aptamer immobilization). Thus, MOF paste represents an ideal platform for developing multiplexed sensing surfaces.

Herein, we report the development of a spatially separated, multiplexed biosensor for sepsis biomarker (PCT, CRP, IL-6) detection. We introduce a three-dimensional (3D) laser-fabricated trimodal sensing platform fabricated on polymethyl methacrylate (PMMA). The device integrates three T-shaped wells incorporating 3-PPA-modified MOF pastes immobilized with DNA aptamers as electroactive sensing layers. We use biomarker-specific amino-functionalized and biotinylated aptamers for selective recognition of IL-6, CRP, and PCT. The system design addresses the key multiplexing challenges, including inadequate compartmentalization, dependence on a shared working electrode, high fabrication complexity, and elevated cost, while integrating signal amplification within a unified sensing platform.

2. Experimental section

Details on the materials, methods, and instrumentation are included in the Supporting Information section.

Fabrication of POC device

A miniaturized multiplexed sensing platform for three biomarkers was fabricated by laser scribing. The platform was designed using AutoCAD software, and the designs were transferred directly to the laser scribing system (Figure 1 and S1). Each working electrode compartment consisted of a T-shaped, two-tiered well, with the central section 3 mm deep and the outer section 2.5 mm deep. A high-power laser was used to engrave these features on the surface of a PMMA substrate measuring 50 × 30 mm, with a thickness of 7 mm. Subsequently, the substrate was patterned to create channels (0.2 mm in depth) to establish electrical connections for electrical measurements. Subsequently, the connection pads were formed using copper tape and fixed with cyanoacrylate adhesive.

Formulation of MOF active paste

View Article Online
DOI: 10.1039/D6TB00732E

Synthesis of MOFs: The MOFs were synthesized as previously reported.[14] A typical synthesis procedure was as follows:

Synthesis of Cu_x Zn_y (Try)_x. Trypan blue (Try) (100 μL) and Cu $(NO_3).2H_2O$ (100 mg), $Zn(NO_3).2H_2O$ (100 mg) were dissolved in 3 mL of dimethylformamide (DMF) and sonicated for 15 min, then heated at 110 °C for 24 h. The product was collected by centrifugation, washed repeatedly with ethanol to remove unreacted precursors and residual ions, and then dried under vacuum at 100 °C for 12 h. Additional synthetic optimization details are included in the Supporting Information (ESI) section.

Post-synthesis functionalization with 3-PPA and paste formulation

The synthesized MOFs were subsequently modified with 3-PPA. Functionalization was carried out by dispersing the MOFs in a 0.1 M aqueous solution of 3-PPA under sonication for approximately 40 min, followed by washing with ethanol and drying at 70–80 °C. The resulting powder was used for electrode paste preparation. 1 mg of this powder was thoroughly mixed with a defined quantity of mineral oil, and the resulting paste was stored at room temperature for further processing.

Fabrication of aptasensor interfaces

Preparation of CRP, IL-6, and PCT sensors with EDC/NHS linkage:

Once the 3-PPA-modified MOF paste was prepared, it was treated with a freshly prepared 1-ethyl-3-(3-dimethylaminopropyl) carbodiimide hydrochloride (EDC) and N-hydroxysuccinimide (NHS) mixture. EDC (0.2 M) and NHS (0.05 M) were each dissolved separately in 50 mM MES buffer (pH 5.5), combined, immediately deposited onto the MOF paste surface, and incubated for 30 min. The activated surfaces were later rinsed with MES buffer and dried under a gentle stream of nitrogen. The resulting activated ester groups were available for covalent conjugation with biorecognition elements. For the CRP sensor, the capture probe consisted of an oligonucleotide bearing a 5' Amino Modifier C6, which was diluted to 1 mM in PBS (pH 7.2). Similarly, for the IL-6 sensor, a 5' Amino Modifier C12 oligonucleotide probe was employed. For the PCT sensor, 3'-biotinylated oligonucleotides were used as the affinity probe.

With amino-modified aptamers, EDC/NHS-activated electrode surfaces were further treated with probe solutions for 2 h. As a result, the immobilization of the respective aptamer was achieved via covalent amide linkage, forming amide bonds between the amine groups of the aptamer and the activated NHS ester. In the case of the biotin-modified aptamer, EDC/NHS-linked surfaces were further treated with streptavidin (STV). The solution (1 mg mL^{-1}) of streptavidin (SA) was prepared in PBS by gentle mixing and diluted to 0.1 mg mL^{-1}. The streptavidin-treated paste was subsequently incubated with the PCT-specific aptamer for 2 h. This step was followed by treatment with bovine serum albumin (BSA) solution for blocking non-specific binding sites, and the modified paste was incubated for approximately 20 h. After the bioconjugation step, the paste was rinsed with 1 mL of PBS, dried, and stored for electrochemical testing.

View Article Online
DOI: 10.1039/D6TB00732E

Electrochemical measurements

The MOF paste-based aptasensors were loaded into the 3 mm central wells and designated as working electrodes, with copper tape serving as the electrical contact at the base. A silver wire reference electrode and a platinum wire auxiliary electrode were positioned in the outer sections to complete a three-electrode electrochemical cell configuration. The copper pads on the edge were connected to the potentiostat for electrochemical measurements. The portions of copper tape potentially exposed to working solutions were insulated to avoid unwanted electrochemical interference. Preliminary electrochemical characterization of unmodified and modified pastes was performed at each fabrication step using glass capillary electrodes. These materials were loaded in the same manner as the well electrodes to form paste electrodes for comparative evaluation. A potential window of -0.3 to 1.2 V and a scan rate range of 0.01–0.3 V s^{-1} were utilized to record the CV cycles.

The initial potential was set to the open circuit voltage for impedance studies over a frequency range of 0.1 Hz to 100 kHz. Impedance spectra were obtained with an AC perturbation amplitude within the range of 0.01–0.035 V. All three sensors were evaluated in PBS (pH=7.4). The developed multiplex platform was subsequently tested using spiked whole blood samples. The test solutions were prepared by mixing 5 µL of PCT (1–100 pg mL^{-1}), CRP (0.001–0.5 mg/mL), and IL-6 (0.01–50 pg mL^{-1}) volumes, which were added to commercially sourced bovine blood samples. The analytical performance of the aptasensors was evaluated using parameters such as active electrode surface area, surface coverage, charge transfer resistance, electron transfer rate constant, sensitivity, and limit of detection (LOD). Furthermore, the cross-reactivity analyses were carried out by mixing equal volumes (20 µL each) of PCT, CRP, and IL-6 analytes. This mixture (15 µL) was applied while recording the signals for each aptasensor, and the electrochemical signals were recorded to assess signal interference arising from non-specific molecular interactions.

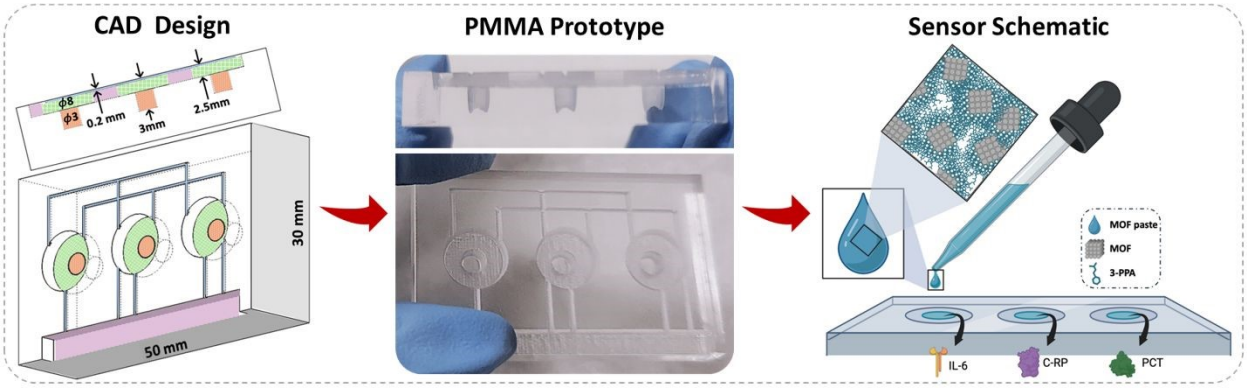

Figure 1. Graphic representation showing the assembly of the PMMA-based layout and the corresponding development of aptasensors.

View Article Online
DOI: 10.1039/D6TB00732E

3. Results and discussion

This work focuses on the miniaturization and integration of ultrasensitive biomarker detection into a single, multiplex point-of-care platform. We developed a handheld PMMA-based laser-engraved miniature device capable of preventing molecular interference and enabling multiplex molecular detection on the same interface.[17] The stepwise fabrication of the device and aptasensor articulation are demonstrated in Figure 1.

3-PPA modified MOF characterization and impedimetric optimization

The surface of the Cu/Zn-TB MOF was modified with 3-PPA to incorporate terminal carboxylic acid groups and to ensure strong metal–phosphonate coordination.[18] The phosphonate linkages with metal centers prevented desorption during the electrochemical measurements. In addition, the introduction of acid functionalities rendered the exposed MOF surface suitable for aptamer attachment via subsequent EDC/NHS-mediated coupling. The morphological changes before and after 3-PPA modification were examined by scanning electron microscopy (SEM). Micrographs of pristine MOFs (Figure 2a and S2) exhibited a non-uniform surface, with irregularly aggregated crystallites and polymorphic features; these results were in agreement with our previous findings. In contrast, 3-PPA-functionalized MOF (Figure 2b) showed a significantly more uniform and interconnected structural network. This transformation in surface morphology suggests a robust coordination of phosphonate groups with metal nodes, leading to improved surface coverage.[17] The N_2 adsorption–desorption study revealed a type II isotherm and a surface area of around 24 $m^2\ g^{-1}$, suggesting the predominantly microporous character (Figure 2c). The large adsorption at higher relative pressures demonstrated a well-developed pore structure in the modified MOF. FTIR spectra exhibited characteristic peaks at 1661.4 cm^{-1} (C=O stretch), 1588.6 cm^{-1} (conjugated C=C stretch), and 1493.1 cm^{-1} (aromatic C=C ring stretch). Further, the C–H out-of-plane bending bands observed at frequencies 880.3 cm^{-1}, 814.7 cm^{-1}, 770.4 cm^{-1}, 688.5 cm^{-1}, are characteristic of substituted aromatic rings of trypan blue.[14]

The XPS analysis of Cu 2p for Cu in Cu/Zn-TB MOF displayed the deconvoluted Cu 2p3/2 and Cu 2p1/2 peaks at 936.6 and 957.4 eV (Figure 2e). Satellite peaks at 943.1, 947.2, and approximately 965.8 eV were also observed, suggesting a change in chemical environment and oxidation state compared to the standard reference material. This is likely attributable to the hybrid composition of the bimetallic MOF and strong interactions with neighboring elements. The Zn 2p spectrum exhibited two well-resolved peaks at 1022.7 (Zn 2p3/2) and 1045.7 eV (Zn 2p1/2), characteristic of Zn^{2+}.[14] The peak separation of approximately 23 eV corresponds to the +2 oxidation state of zinc (Figure 2f) and further suggests the coordination with the O and N atoms and the retention of a typical tetrahedral coordination geometry. The XRD analysis revealed sharp diffraction peaks at $2\theta = 10.21$, 10.81, 16.19, 17.07, and 24.82, corresponding to (100), (101), (111), (211), and (222) crystallographic planes, respectively (Figure 2g). The phase analysis indicated that the MOF comprises a mixture of nearly 60% monoclinic and 40% triclinic phases.[14]

View Article Online
DOI: 10.1039/D6TB00732E

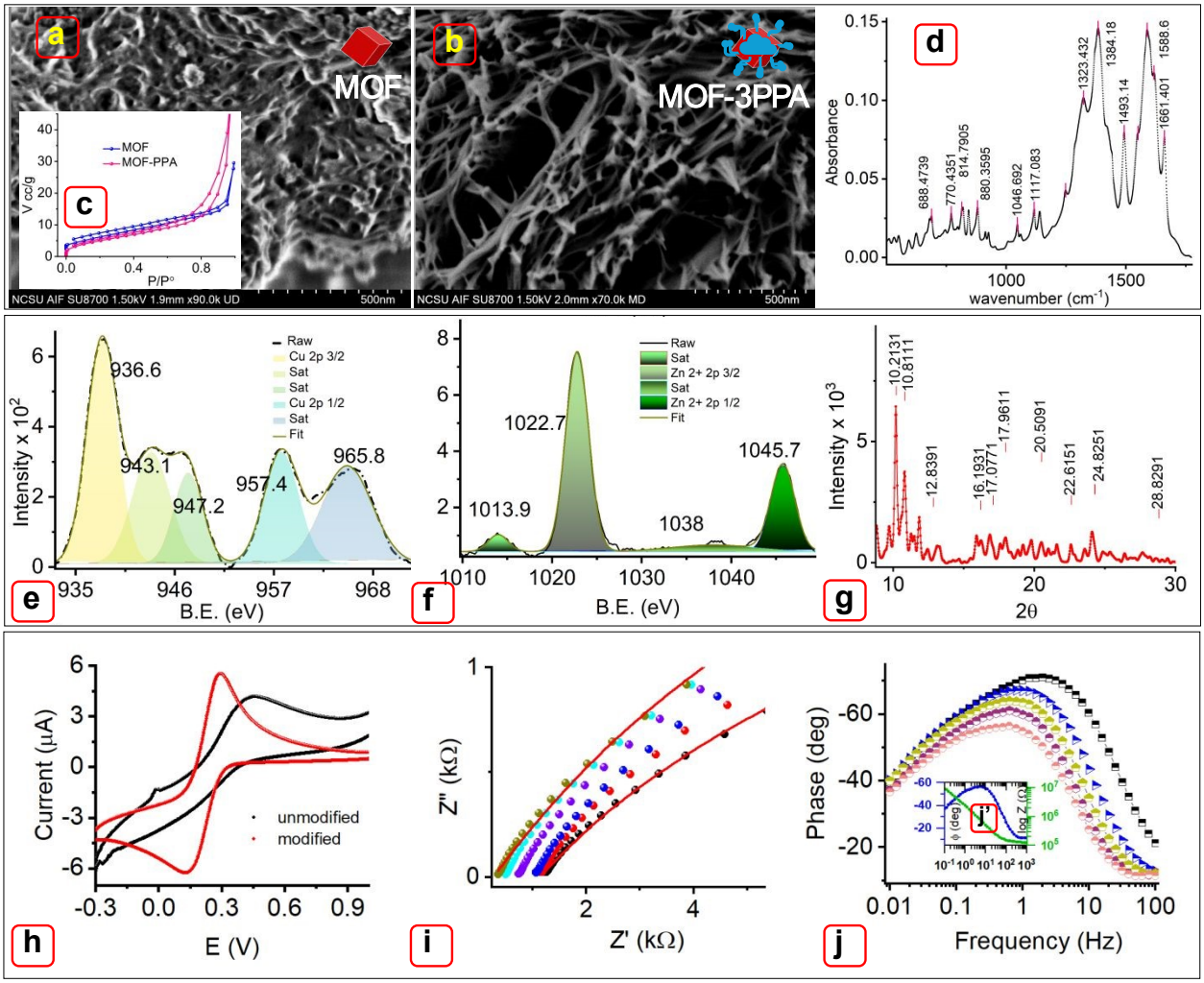

Figure 2. SEM micrographs before (a) and after (b) modification of MOF with 3-PPA. (c) N_2 adsorption isotherms, (d) FTIR spectra, XPS profile of (e) Cu 2p, (f) Zn 2p, (g) X-ray diffractogram of Cu/Zn-TB MOF. (h) Comparison of electrode behavior upon 3-PPA introduction into the MOF matrix. Nyquist (i) and frequency vs phase (j) plots showing the optimization of 3-PPA concentration in the MOF. The inset picture (j') shows the corresponding Bode plot.

The electrochemical behavior of unmodified and modified MOFs as pastes was evaluated (Figure 2h). The cyclic voltammogram data revealed significant changes in the redox reversibility after 3-PPA treatment. The as-synthesized MOF exhibited less distinct redox peaks, suggesting sluggish electron-transfer kinetics and non-uniform surface states. As recorded in a previous study, unmodified MOF pastes exhibited well-defined oxidation peaks (Figure 2h), accompanied by poorly resolved reduction peaks at 0.44 and 0.14 V.[14] 3-PPA-modified MOFs showed well-defined cathodic and anodic peaks with reduced peak separation. The redox reversibility was substantially improved, with peaks appearing at lower potentials of 0.35 and 0.08 V, along with a reduced lower peak separation of 0.16 V (compared to ~ 0.32 V on blank paste). The reduction in current density

View Article Online
DOI: 10.1039/D6TB00732E

increased, while the oxidation current density did not increase significantly. This may be attributed to the integration of phosphonic acid functionalities, which enhanced the hydrophilicity of the surface and promoted more efficient electron delocalization. The symmetrical anodic and cathodic current response indicated rapid electron transfer kinetics. This is also a characteristic feature of enhanced carrier mobility at the electrode-electrolyte interface. The enhancement in current magnitude is attributed to the increase in electroactive surface area and better charge carrier intensity. Additionally, the mixed valence (Cu^{+}/Cu^{2+}) of Cu metal centers is the primary pathway for charge carriers via hole hopping.

The surface modification with 3-PPA was then optimized using impedance spectroscopy analysis (EIS). The Nyquist plots shown in Figure 2i clearly show the dependence of Rct on the concentration of 3-PPA used for surface modification. The MOFs were modified with varying 3-PPA concentrations (0.01–0.5 M). The semicircular arc profiles of each MOF-PPA paste electrode are represented by distinct color markers (Figure 2i). The Rct values vary from 1275 Ω for the unmodified MOF electrode (black symbol) to 350 Ω for MOF-PPA incorporated with 0.5 M. This finding reflects a substantial reduction in charge transfer resistance values and suggests the formation of a more electroactive surface. The arcs were fitted using an equivalent circuit model, confirming the reliability of the impedance data collected for all systems. Bode plots (Figure 2j) for all compositions demonstrated similar response curves, with minimal variation in phase values. Across the frequency range of 10^{4}–10^{1} Hz, most spectra (e.g., Figure 2j') exhibited slopes between –0.651 and –0.785, which is indicative of a quasi-Warburg response. This finding indicates the contributions from ion diffusion within pores, heterogeneous charge transfer, and a non-ideal capacitive response.[19–20] Moreover, the phase angles between –30 and –70 ° suggest that the electrode exhibits predominantly capacitive features. These results can be attributed to the introduction of phosphonic acid groups, which enhance electrolyte penetration, improving surface wettability, and facilitating charge accumulation. [19–20]

View Article Online
DOI: 10.1039/D6TB00732E

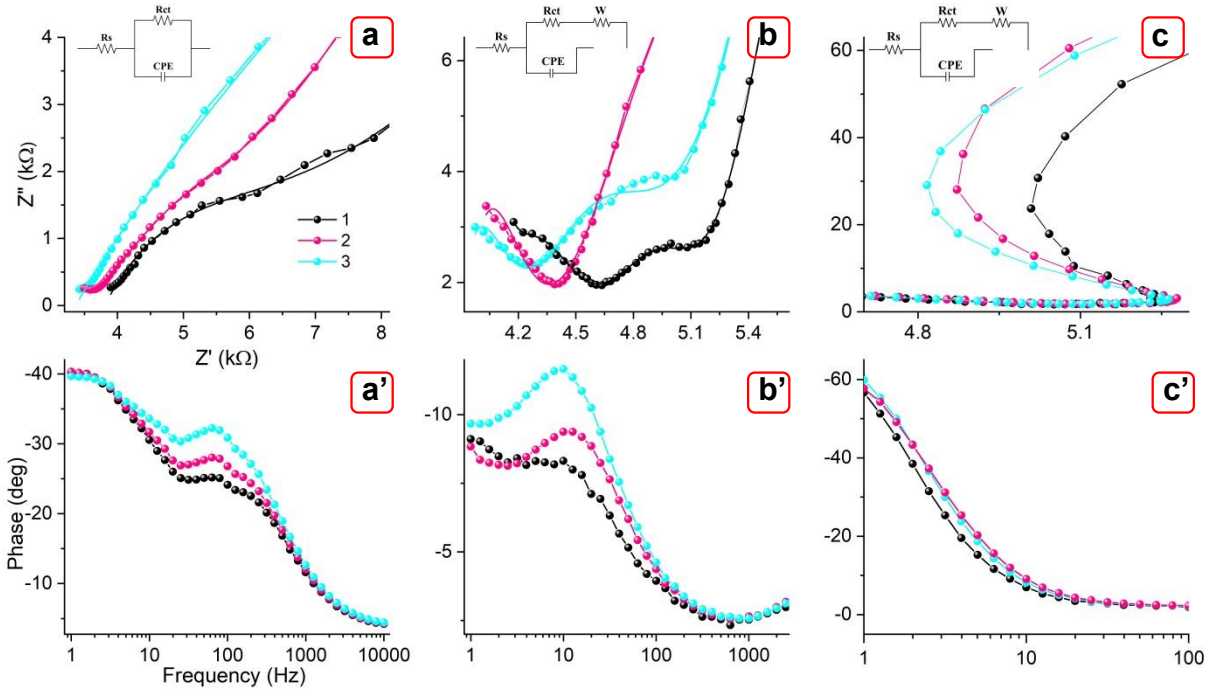

Figure 3. EIS time-dependent monitoring of the aptamer immobilization process. Nyquist impedance spectrum with fitted curves and corresponding frequency plots, recorded after 15-20 minutes of soaking time in (a-a') EDC/NHS solution, (b-b') aptamer solution, and (c-c') upon biomarker coupling. Inset images in Figure (a-c) represent the equivalent circuit used in fitting the data.

Impedimetric evaluation of aptamer immobilization

Here, we monitored time-dependent surface functionalization of MOFs during incubation in EDC/NHS, and subsequently upon incubation in aptamer solutions for PCT, CRP, and IL-6 using the EIS technique. Figure 3a-c and 3a'-c' display the Nyquist and corresponding Bode plots collected at 15-minute intervals during each treatment step. The spectra (Figure 3a) revealed a gradual increase in arc diameter, resulting in a steady increase in charge transfer resistance (Rct) values after EDC/NHS treatment.[21] The behavior is likely attributable to the activation of carboxylic acid (–COOH) groups and their conversion into O-acylisourea and NHS-ester intermediates, forming resistive interfacial layers at the electrode-electrolyte interface.[21] Similarly, the corresponding Bode plots (Figure 3a' and Figure S4) show a significant rise in impedance magnitude (|Z|) from mid to low frequency range (10^4–10^1 Hz), with a marked increase in the Rct values. The slope values range from –0.218 to –0.411, reflecting the consistent quasi-capacitive behavior.[21] The phase angle values are initially observed (~ ϕ = -5 to -20°) in the mid frequency region (10^4–10^2), and later shifted to –45° in the low frequency region. The mixed values in the mid-frequency region suggest that the interface has mixed capacitive (C) and resistive (R) qualities, while the latter values reflect balanced RC behavior consistent with Warburg or constant phase element (CPE). Overall, these results confirm progressive and effective surface

View Article Online
DOI: 10.1039/D6TB00732E

functionalization. Both diffusion and charge transfer processes contribute substantially to the overall impedance response.

Similarly, the spectra recorded after incubation in the aptamer solution indicate the successful immobilization of specific aptamers via amide bond formation with NHS-ester intermediates. In agreement with previous findings, the Nyquist plots transition toward a more vertical trajectory, and the Rct values reach a plateau (Figure 3b), suggesting full surface coverage, limiting ion diffusion to the electrode surface.[21] This behavior confirms the formation of a dense, resistive aptamer layer. The equivalent circuit models fitted to the EIS data are shown in Figure 3a-c. The EDC/NHS-treated surface consists of an electrolyte/solution resistance (Rs), a charge transfer resistance (Rct), and a constant phase element (CPE). Both the aptamer-modified surface and the post-analyte-binding stage were modeled using an open circuit with an additional component, a Warburg element (W_0). This was incorporated to model the linear low-frequency response and represent analyte diffusion.

The corresponding Bode plots show a gradual increase in |Z| values over mid frequencies, and a sharp increase in impedance magnitude at lower frequencies (Figure S5). The phase curve exhibits a characteristic phase response from mid to low frequencies, with a shift from approximately –2 to –10°. The increase in low-frequency impedance, together with a shift in phase angle, reflects progressive blocking of electron transfer and surface saturation. Subsequently, the spectra were recorded in the presence of the biomarker solution. The Nyquist curves exhibit two distinct regions: a semicircular high-|Z| and a linear low-|Z| region (Figure 3c). The larger arc diameter reflected elevated Rct, confirming that aptamer-biomarker binding impeded charge transfer. The quasi-linear portions at low frequencies indicated diffusion-controlled behavior. The Bode plot shows the shift in phase angle from ~ 0° (higher frequency) to -60° (lower frequency), indicating a transition from solution-resistance dominance at high frequencies to the formation of an insulating biomarker layer at the electrode-electrolyte interface (Figure 3c' and Figure S6). The slope value of –0.017, approaching zero, further confirms the resistive behavior. These characteristics suggest the formation of a resistive aptamer-biomarker complex, and are consistent with findings reported by Ruankham et al. and Oliveira et al.[21–22]

Voltammetric evaluation of aptasensors

In this study, the electron transfer arises from the intrinsic redox activity of the TB ligands integrated within the MOF paste, rather than by an external redox probe.

View Article Online
DOI: 10.1039/D6TB00732E

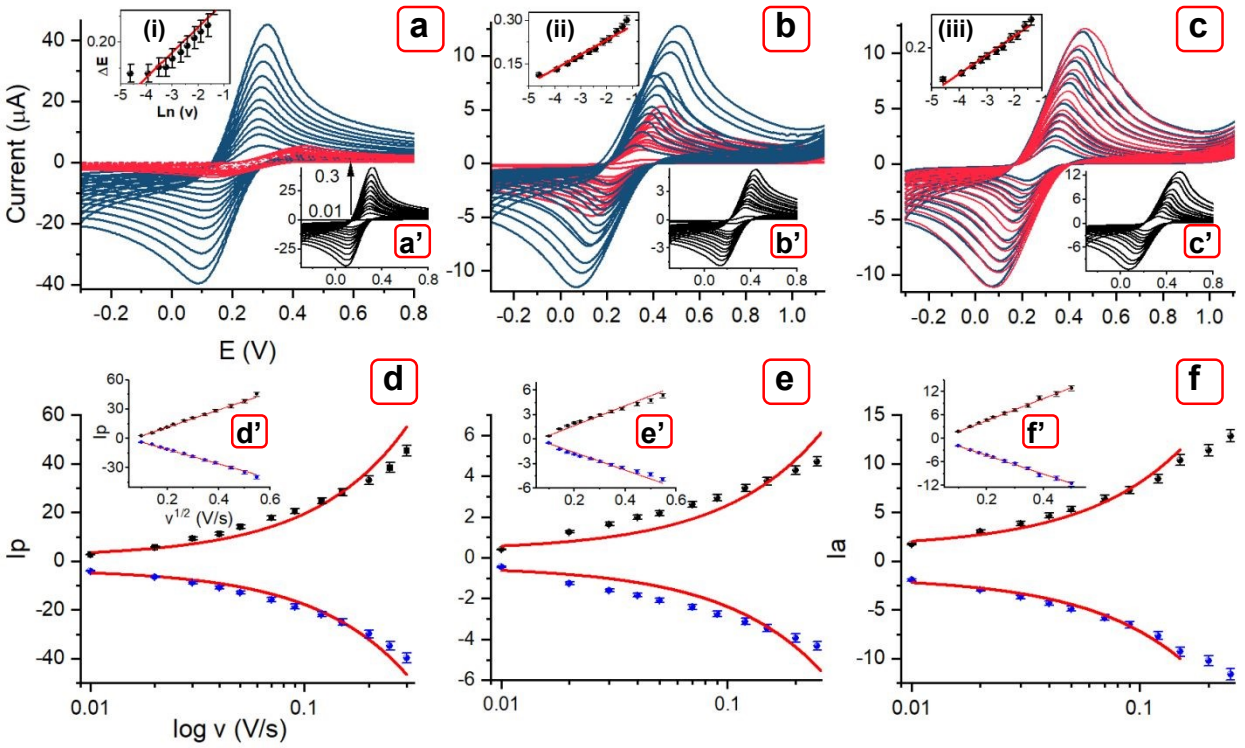

Figure 4. CVs depicting the effect of variable scan rates (0.01-0.3 Vs^{-1}) on reversibility in overlapped, (a) MOF-PPA and PCT aptamer, (b) PCT aptamer and after biomarker coupling (PCT - 1 pg mL^{-1}), and (c) different concentration curves (PCT - 1 & 5 pg mL^{-1}). Inset pictures represent the CVs for MOF-PPA (a'), PCT aptamer (b'), 1 pg mL^{-1} curves (c'), and Ep vs. ln v plots (i-iii). Calibration plot of Ip (anodic (a), cathodic (c)) vs. log v for (d) MOF-PPA and PCT aptamer, (e) PCT aptamer, and (f) after biomarker coupling (PCT - 1 pg mL^{-1}). Insets (d'-f') are corresponding plots of Ip (a, c) vs. the square root of scan rate ($v^{1/2}$).

The conjugated azo/quinonoid groups of TB in the MOF-TB paste loaded into the PMMA serve as reversible redox-active centers. As reported in our previous work on TB-linked MOFs synthesis, the characteristically low charge mobility values ($\mu < 0.1$ $cm^2V^{-1}s^{-1}$) indicate that charge transport proceeds primarily via a hopping mechanism.[14] This is consistent with the methodology reported by Irimes et al., in which voltammograms were recorded with reference to the ferrocene (Fc) redox signal.[23] Here, the three working electrodes were designated as WE1, WE2, and WE3 for PCT, CRP, and IL-6 detection, respectively. Figure 4–6 presents the cyclic voltammetric (CV) responses characterization of three paste electrodes over a potential range of –0.3 to 1.2 V. The electrochemical behavior of three electrodes was evaluated at each modification step: carboxylic acid functionalization with 3-PPA, EDC/NHS surface activation, and subsequent aptamer immobilization. Following EDC/NHS treatment of the 3-PPA-functionalized surface, the redox reversibility was further improved across all electrodes. The peak current responses increased substantially, and a significant negative shift in potential of approximately 0.2 V was observed.

View Article Online
DOI: 10.1039/D6TB00732E

For PCT detection, WE1 was immersed in streptavidin solution, and the peak currents approximately doubled (Figure S7). After PCT, CRP, and IL-6 specific aptamer immobilization, the peaks shifted to lower anodic/cathodic peak potentials (0.23 / 0.003 V for PCT, 0.25 / 0.04 V for CRP, and 0.12 / 0.02 V for IL-6).

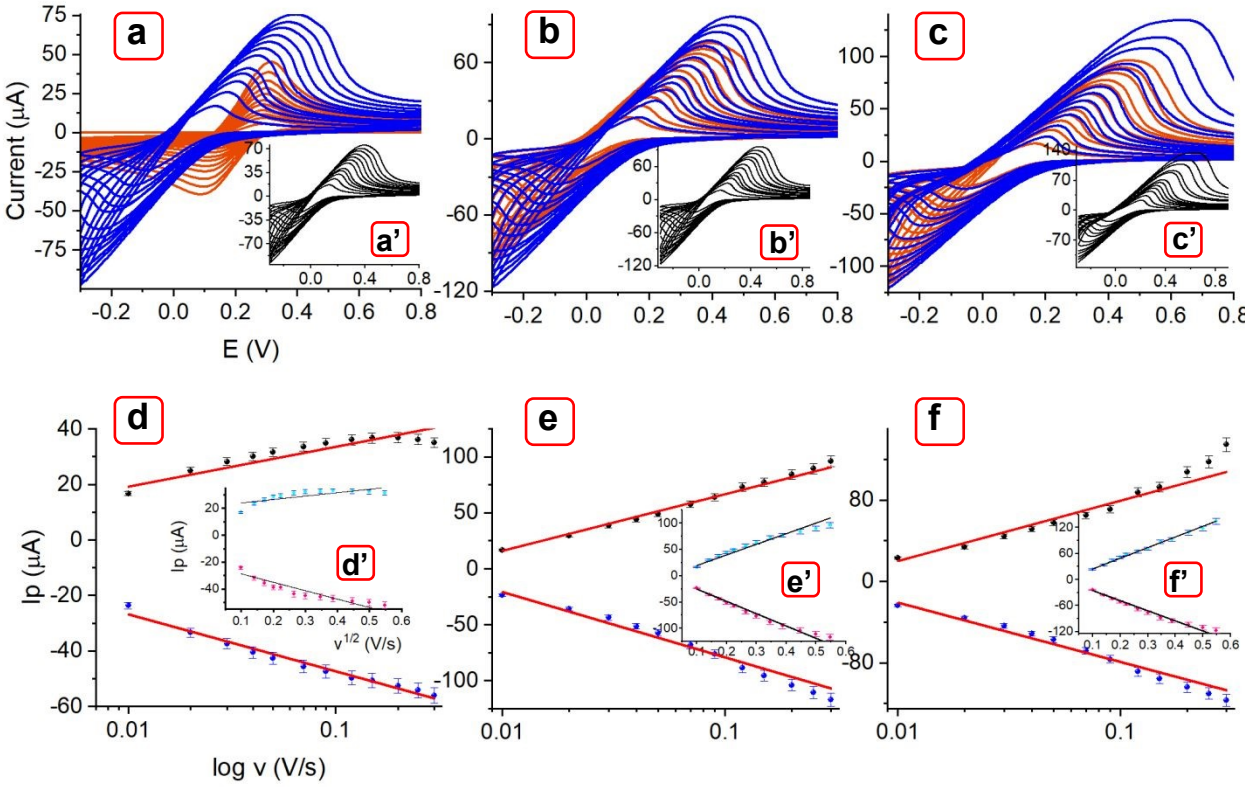

Figure 5. CVs depicting the effect of variable scan rates (0.01-0.3 Vs^{-1}) on reversibility in overlapped, (a) MOF-PPA and CRP aptamer, (b) CRP aptamer and after biomarker coupling (CRP - 0.001 mg mL^{-1}), and (c) different concentration curves (CRP - 0.001 mg mL^{-1} & 0.5 mg mL^{-1}). Inset pictures represent the CVs for (a') CRP aptamer, (b') 0.001 mg mL^{-1}, and (c') 0.5 mg mL^{-1} curves. Calibration plot of Ip (anodic (a), cathodic (c)) vs. log v for (d) MOF-PPA and CRP aptamer, (e) CRP aptamer, and (f) after biomarker coupling (CRP - 0.001 mg mL^{-1}). Insets (d'-f') are corresponding plots of Ip (a, c) vs. $v^{1/2}$.

The successful aptamer immobilization resulted in a further decrease in peak separation and a proportionate increase in peak current responses. Upon recording voltammograms in the presence of 10 nM solutions of the respective biomarkers, the peak currents increased accordingly. Notably, in the case of WE3, there was a significant shift in peak potential of approximately 0.1 V, a two-fold increase in oxidation and reduction currents. Additionally, voltammetric responses were recorded over a range of scan rates 0.01 V/s–0.3 V/s (Figures 4-6a-c) to examine the aptamer

View Article Online
DOI: 10.1039/D6TB00732E

surface coverage, interfacial changes at the working electrode surface in terms of electrode kinetics, and variations in electrochemically accessible area following aptamer conjugation and biomarker binding. Figure 4a' shows the scan rate (v) dependent voltammograms for MOF-PPA, aptamer modified WE1 (Figure 4b'), WE2 (Figure 5a'), and WE3 (Figure 6a'), and following the addition of biomarkers PCT (Figure 4c-c'), CRP (Figure 5b'-c'), and IL-6 (Figure 6b'-c'). Key observations include approximately 8- and 4-fold decreases in peak current responses, changes in redox reversibility, following aptamer coupling and biomarker recognition. The transition from a nonlinear Ip vs. v relationship (Figures 4-6d-f) for MOF-PPA to a near-linear trend for subsequent modification steps, accompanied by a shift in Ip vs. $v^{1/2}$ plots towards nonlinear behavior (Figures 4-6d'-f'), indicated a transition from diffusion-controlled to surface-confined electrochemical behavior.

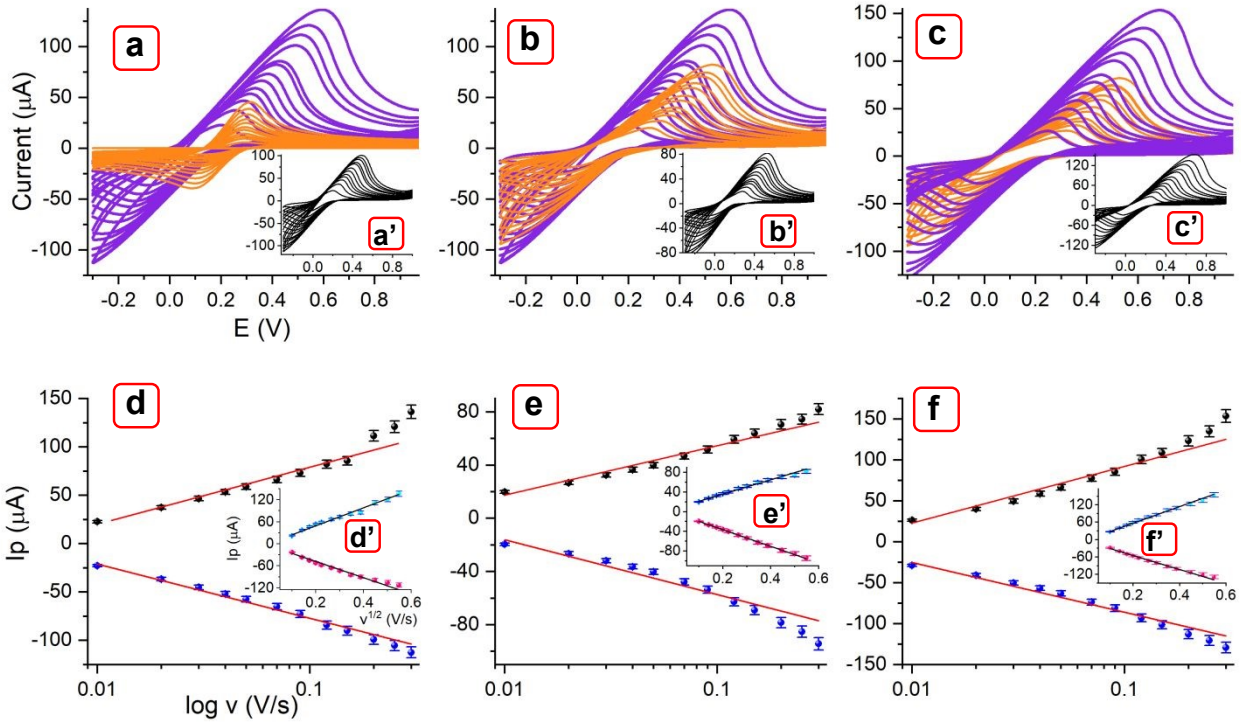

Figure 6. CVs depicting the effect of variable scan rates (0.01-0.3 Vs^{-1}) on reversibility in overlapped, (a) MOF-PPA and IL-6 aptamer, (b) IL-6 aptamer and after biomarker coupling (IL-6 - 0.1 pg mL^{-1}), and (c) different concentration curves (IL-6 - 0.01 pg mL^{-1} & 50 pg mL^{-1}). Inset pictures represent the CVs for (a') IL-6 aptamer, (b') 0.1 pg mL^{-1}, and (c') 50 pg mL^{-1}. Calibration plot of Ip (anodic (a), cathodic (c)) vs. log v for (d) MOF-PPA and IL-6 aptamer, (e) IL-6 aptamer, and (f) after biomarker coupling (IL-6 - 0.01 pg mL^{-1}). Insets (d' - f') are corresponding plots of Ip (a, c) vs. the square root of scan rate ($v^{1/2}$).

The surface-confined electrochemical response upon aptamer immobilization and biomarker linking was calculated using Equation 1. The peak current values were recorded as 1.99 (aptamer), 3.89 (conc1), 4.68 (conc2) μA (WE1), 28.45 (aptamer), 44.01 (conc1), 51.51 (conc2) μA (WE2)

View Article Online
DOI: 10.1039/D6TB00732E

and 53.404 (aptamer), 36.34 (conc1), 58.51 (conc2) μA WE3, respectively, at 0.04 V/s, with an electrode area (A) of 0.070 cm^2.

$$I_p = \frac{n^2 F^2 A \Gamma v}{4RT} \quad \text{(Eq 1)}$$

The corresponding values of surface coverage (Γ) were estimated by integrating the baseline-corrected anodic peak at the slowest scan rate (0.01 V/s) using Eq. 1. Upon PCT aptamer immobilization (WE1), $\Gamma = 1.06 \times 10^{-9}$ mol/cm^2 and upon target binding ($\Gamma = 1.47 \times 10^{-9}$, 1.77×10^{-9} mol/cm^2), which are 10^2-fold lower than that of MOF-PPA ($\Gamma = 1.08 \times 10^{-7}$ mol/cm^2), confirming effective blocking of the electrode surface. Similarly, for CRP (WE2), $\Gamma = 0.03 \times 10^{-9}$ (aptamer), 1.39×10^{-9} (conc1), 1.68×10^{-9} mol/cm^2 (conc2), and for IL-6 (WE3), $\Gamma = 1.01 \times 10^{-8}$ (aptamer), 1.38×10^{-8} (conc1), and 2.22×10^{-8} mol/cm^2 (conc2). This finding indicated that the surface coverage scales proportionally with peak current responses, demonstrating successful aptamer coupling and biomarker binding. This trend is consistent with findings reported by Goda et al.[24]

Additionally, from the Randles – Sevcik's equation:

$$I_p = 2.69\ x\ 10^5 n_2^3\ A\ C\ v_2^1\ D_2^1 \quad \text{(Eq 2)}$$

where Ip is peak current (A), the values of diffusion coefficient (D) were calculated at a scan rate of 0.04 V/s, with an electrode area (A) of 0.070 cm^2 and at two different concentrations (C) of 10 μM and 1 nM (1 x 10^{-12} mol/cm^3). The values were obtained in the range 10^1–10^3, which are significantly higher than the reported D values for purely diffusion-controlled systems (~ 10^{-3}–10^{-6}). This suggests that the system becomes increasingly surface-confined upon successive modification. It is consistent with the fact that trypan blue is incorporated as a structural element during synthesis and acts as an intrinsic redox-active component within the MOF framework. Thus, the system exhibits an apparent diffusion coefficient (D_app).

The dependence of Ep vs. ln v plot was analyzed using the Laviron equation (Eq 3),

$$E_p = E^0 + \frac{RT}{\alpha nF} ln\left(\frac{RTk^0}{\alpha nF}\right) - \frac{RT}{\alpha nF} lnv \quad \text{(Eq 3)}$$

The charge transfer coefficient α and rate constant k^0 were calculated from this equation, at 298 K, with n = 1.

While the Laviron equations for anodic and cathodic peaks:

$$E_{pa} = E^0 + \frac{RT}{(1-\alpha)nF} lnv \quad \text{(Eq 4)}$$

$$E_{pc} = E^0 - \frac{RT}{\alpha nF} lnv \quad \text{(Eq 5)}$$

The charge transfer coefficient (α) was calculated from the anodic slope as:

View Article Online
DOI: 10.1039/D6TB00732E

$$\alpha = 1 - \frac{RT}{nF\ x\ slope_a} \qquad \text{(Eq 6)}$$

MOF-PPA exhibited a low slope of 0.02 V and an intercept (−0.261 V) (Figure 4i), indicating rapid, near-reversible electron transfer kinetics (α=0.50, $k^0 = 0.426 \pm 0.073\ s^{-1}$). Immobilization of PCT (Figure 4ii), CRP (Figure S8a), and IL-6 (Figure S9a) aptamers led to progressive increases in slope values (0.054 V (WE1), 0.145 V (WE2), and 0.192 V (WE3)), indicating progressively slower electron transfer kinetics. Gradual aptamer immobilization systematically reduced the values of α, k^0, PCT (0.476, $0.294 \pm 0.035\ s^{-1}$), CRP (0.177, $0.023 \pm 0.004\ s^{-1}$), and IL-6 (0.134, $0.034 \pm 0.006\ s^{-1}$), confirming the formation of an interfacial barrier layer. The pronounced change observed for the IL-6-modified electrode suggested denser aptamer packing, indicative of denser aptamer packing and a more pronounced kinetic barrier. In the presence of the target biomarkers, the slope values showed clear concentration-dependent kinetics. For PCT, at low concentration (Figure 4iii), the slope increased to 0.075 V (α=0.343, $k^0 = 0.320 \pm 0.047\ s^{-1}$), indicating a significant conformational change in the aptamer upon target binding, and decreased to 0.049 (α=0.524, $k^0 = 0.294 \pm 0.035\ s^{-1}$) at higher concentration, indicating a dose-dependent conformational change and surface saturation. In the case of CRP at both concentrations, equivalent slopes (0.172 V α=0.149, $k^0 = 0.012 \pm 0.006\ s^{-1}$) and intercepts (-0.987 V) were observed; this finding was attributed to saturation binding or similar conformational states (Figure S8b-c). IL-6 studies showed a measurable change in slope from 0.192–0.202 V (α=0.127, $k^0 = 0.036 \pm 0.007\ s^{-1}$), reflecting concentration-dependent conformational changes upon target binding (Figure S9b-c). Overall, the changes in peak separation and electrode surface kinetics were influenced by aptamer density, biomarker coupling, and saturation effects.

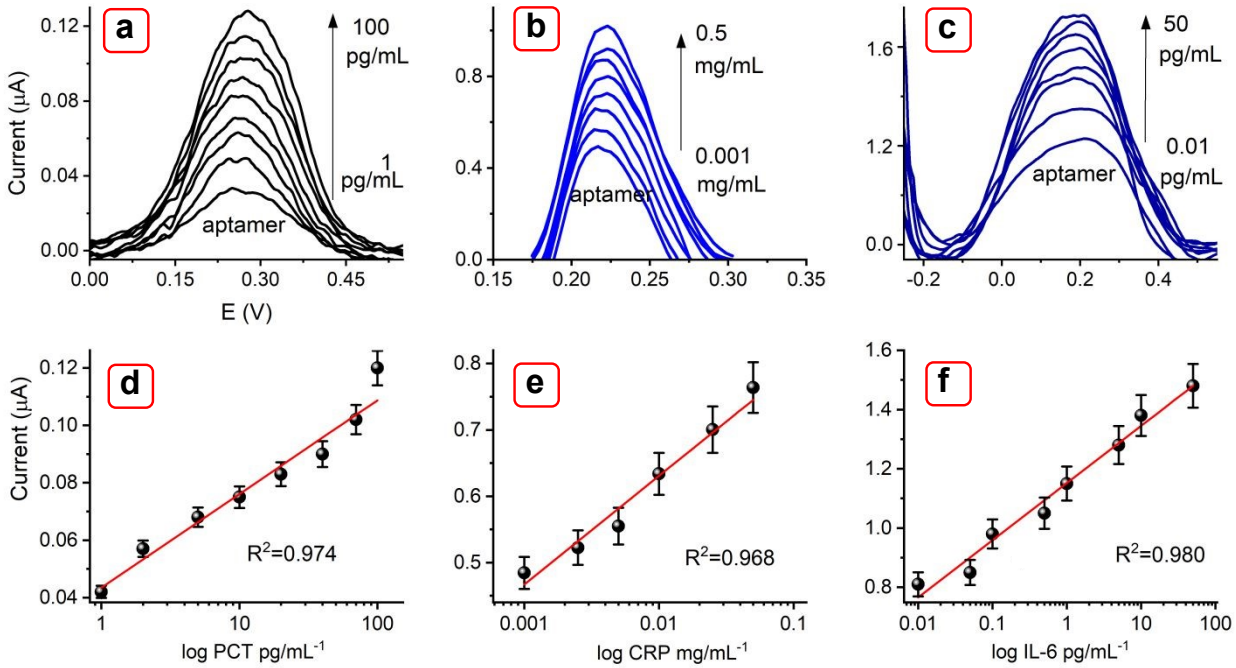

View Article Online
DOI: 10.1039/D6TB00732E

Figure 7. Differential pulse voltammograms of PCT (a), CRP (b), and IL-6 (c) detection. Corresponding Ip vs. concentration calibration plots of (d) PCT (1–100 pg mL^{-1}), (e) CRP (0.001–0.5 mg/mL), and (f) IL-6 (0.01–50 pg mL^{-1})

Evaluation of Aptasensor Sensitivity

The analytical sensitivity of these aptasensors was evaluated using differential pulse voltammetry (DPV). The aptamer-modified surfaces (WE1, WE2, and WE3) were recorded before and after the addition of the target biomarkers (PCT, CRP, and IL-6). The DPV signals were recorded within the potential window corresponding to MOF-TB oxidation peaks, as identified across the different electrode interfaces as determined from CV measurements. Figure 7a-c shows the DPV results for the WE1, WE2, and WE3 electrochemical aptasensors in 0.1 M PBS (pH 7.4), consistent with the approach reported by William et al. for aptasensor-based detection of CRP levels.[25] Voltammetric responses were recorded upon successive addition of the target biomarkers. The current responses scaled proportionally with increasing biomarker concentrations. In the case of WE1, a positive potential shift from 0.216 to 0.232 V was observed upon aptamer-PCT binding. The signal increased gradually with increasing PCT levels, ranging from 1–100 pg mL^{-1} (Figure 7d). This behavior may be attributed to conformational changes in the aptamer upon target binding. For CRP detection on WE2, the peak current increased progressively across the range of 0.001–0.5 mg mL^{-1} (Figure 7e). Likewise, DPV signals recorded for IL-6 detection on WE3 showed a concentration-dependent increase in peak current over a range of 0.01–50 pg mL^{-1} (Figure 7f). The detection limits were calculated as 0.204 pg mL^{-1} (R^2 = 0.97, PCT, WE1), 0.02 mg mL^{-1} (R^2 = 0.99, CRP, WE2), and 0.315 pg mL^{-1} (R^2 = 0.96, IL-6, WE3) based on linear regression analysis. The corresponding sensitivity values were obtained as 0.461 µA/pg $mL^{-1}cm^2$ (PCT), 2.3 µA/mg mL^{-1} cm^2 (CRP), and 2.730 µA/pg $mL^{-1}cm^2$ (IL-6), demonstrating the sensor's capability for trace-level detection in complex matrices. These sensitivity values were normalized to the working electrode area. The obtained LOD values fall well within the tested concentration ranges, confirming the high sensitivity of the platform. The observations are consistent with the findings of Tseng et al., who reported PCT aptasensing using a similar oligonucleotide sequence.[26] Furthermore, the MOF-paste electrode with probe modifications constitutes a highly responsive interface for point-of-care diagnostic applications.

View Article Online
DOI: 10.1039/D6TB00732E

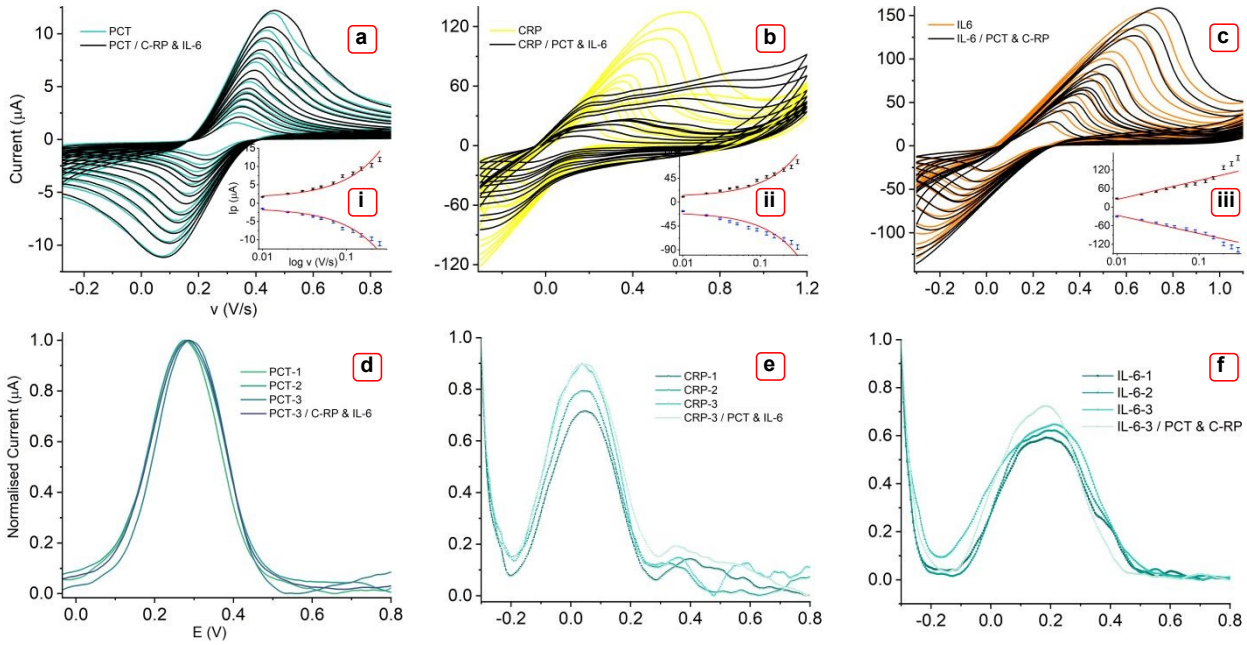

Figure 8. The scan rate (0.01–0.3 Vs^{-1}) dependent overlapped CVs and DPVs of (a, d) PCT and PCT + IL-6 + CRP, (b, e) CRP and CRP + IL-6 + PCT, and (c, f) IL-6 and IL-6 + CRP + PCT. Inset pictures (i-iii) represent the calibration plot of Ip (a, c) vs. log v for these CVs.

Cross-reactivity analyses for aptasensors

The molecule recognition capability of the fabricated aptasensors was assessed by evaluating cross-reactivity by exposing each electrode to non-target biomarkers. The effect of CRP (0.5 mg mL^{-1}) and IL-6 (50 pg mL^{-1}) on PCT detection (WE1) was evaluated using CV and DPV measurements. Similarly, the effect of PCT (100 pg mL^{-1}) and IL-6 (50 pg mL^{-1}) on CRP (WE2), and the effect of PCT (100 pg mL^{-1}) and CRP (0.5 mg mL^{-1}) on IL-6 (WE3) were assessed.[22] Figure 8 presents the comparison of CV and DPV curves before and after spiking with non-target biomarkers. Peak current responses and oxidation potential values in the CV and DPV scans did not deviate significantly from control conditions (Figure 8a-e). Notably for CRP, the redox response showed further attenuation, which may be attributed to surface saturation upon target binding (Figure 8b). The surface coverage values obtained from the respective Ip vs. log v plots (Figure 8i-iii) include 1.7×10^{-9} mol cm^{-2} (PCT), 2.8×10^{-9} mol cm^{-2} (CRP), and 2.3×10^{-8} mol cm^{-2} (IL-6). These values are comparable to those reported previously obtained at the upper limit of concentration (1.77×10^{-9} mol/cm^2 (WE1), 1.68×10^{-9} mol/cm^2 (WE2), and 2.22×10^{-8} mol/cm^2 (WE3)), with a negligible deviation of approximately 5%. Furthermore, the slope values from Ep vs. ln v plots of 0.054 (WE1, PCT), 0.18 V (WE2, CRP), and 0.22 V (WE3, IL-6) were comparable to those from individual assays (0.049 (PCT), 0.172 V (CRP), and 0.202 V (IL-6)) at the same concentrations, confirming low cross-reactivity (Figure S10). This finding demonstrates that the aptamer-biomarker interactions are stable and selective, consistent with results reported by

View Article Online
DOI: 10.1039/D6TB00732E

Whitehouse et al., who demonstrated minor cross-reactivity in aptasensor-based detection of CRP.[25]

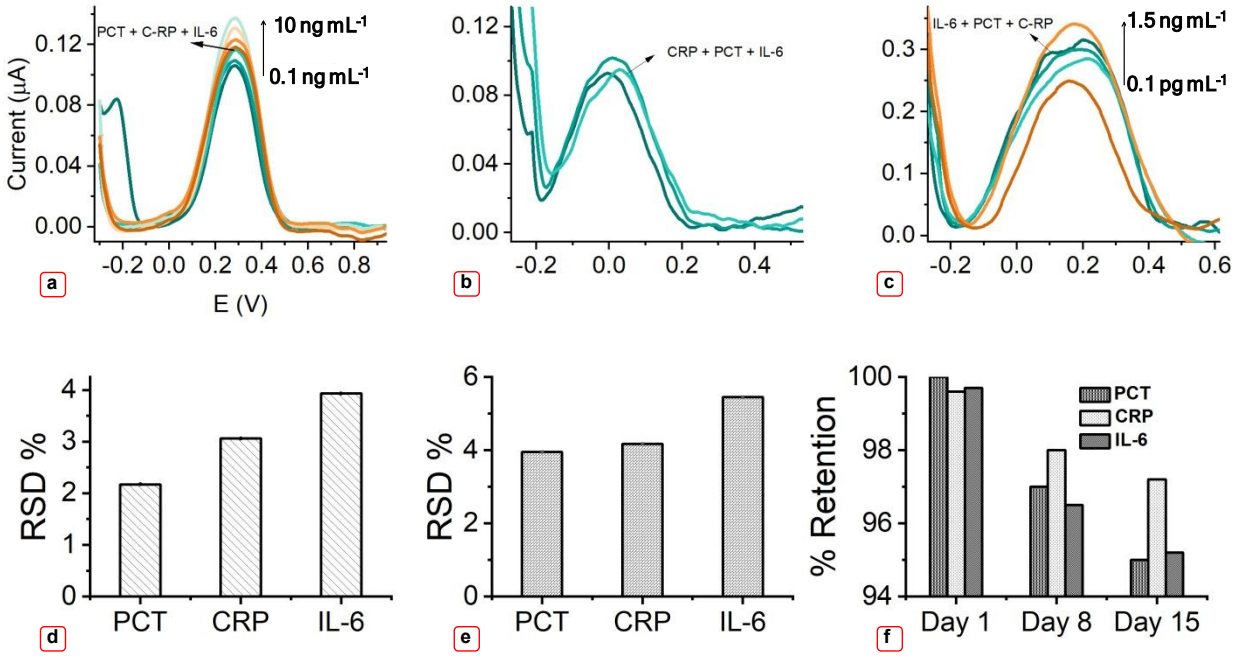

Figure 9. DPVs of spiked blood samples with the standard concentrations (a) PCT, (b) CRP, and (c) IL-6. Bar graphs showing the (d) repeatability, (e) batch-to-batch reproducibility, and (f) stability of aptasensors.

Performance validation with spiked biological samples

The capability of the developed trimodal aptasensor platform to detect the biomarkers in a complex biological matrix was evaluated. The commercially obtained blood was diluted in PBS and spiked with physiologically significant concentrations of PCT (1 pg mL^{-1}), CRP (0.5 mg mL^{-1}), and IL-6 (0.01 pg mL^{-1}) within clinically relevant healthy ranges under ambient measurement conditions. Additionally, the cross-reactivity was evaluated in the blood samples (Figure 9a-c). The peak current responses were in good agreement with those of solution experiments, and signals arising from cross-reactive species remained within comparable potential regions (Figure 9a-c). These results demonstrate that the developed aptasensor platform enables efficient biomarker detection in complex blood matrices. However, certain limitations remain; fully integrated device designs are required for more effective POC applications, and real-time monitoring of aptamer conformational dynamics warrants further investigation.

The repeatability of the aptasensors was evaluated from five consecutive measurements, yielding %RSD values of 2.17%, 3.06%, and 3.93% for PCT, CRP, and IL-6, respectively (Figure 9d). Batch-to-batch reproducibility was assessed across three independently fabricated sensors, which

View Article Online
DOI: 10.1039/D6TB00732E

yielded %RSD values of 3.95%, 4.17%, and 5.45% (Figure 9e). Storage stability was further assessed over 2 weeks at 4°C, and the sensors retained 95.53%, 97.35%, and 97.02% of their initial signal responses for PCT, CRP, and IL-6, respectively, on Day 15 (Figure 9f). These results indicated a shelf life of at least 15 days.

4. Conclusions

In summary, we have reported a cost-effective approach for the sensitive and selective detection of sepsis biomarkers. A laser-patterned, trimodal multiplex electrochemical aptasensing platform was designed for the selective detection of PCT, CRP, and IL-6 levels. The MOF-PPA paste electrodes exhibited excellent electrical conductivity and supported stable aptamer immobilization. Following careful optimization, probe-biomarker binding produced well-defined voltammetric and impedance signals, without cross-contamination. The platform achieved clinically relevant detection thresholds for 0.204 pg mL^{-1} (PCT), 0.02 mg mL^{-1} (CRP), and 0.315 pg mL^{-1} (IL-6), with high sensitivity and negligible cross-reactivity with non-target biomarkers; the results were validated against physiologically relevant levels in spiked solutions and blood samples. These findings suggest that the developed devices could serve as viable alternatives to conventional laboratory-based diagnostics for POC-based biomedical applications.

Author Contributions

S. S. performed all the experiments, did data interpretation and calculations, wrote the manuscript; S.S.S. helped with laser designing on PMMA, and procured SEM data. S. K. reviewed the manuscript draft. M.M. helped with the schematic illustrations. R. J. N. procured the funding, supervised throughout, and reviewed the draft.

Acknowledgments

This effort is sponsored by the Government under Other Transaction Number W81XWH-15-9-0001.

Disclaimer: The views and conclusions contained herein are those of the authors and should not be interpreted as necessarily representing the official policies or endorsements, either expressed or implied, of the U.S. Government.

View Article Online
DOI: 10.1039/D6TB00732E

References

1. Kumar, A.; Roberts, D.; Wood, K. E.; Light, B.; Parrillo, J. E.; Sharma, S.; Suppes, R.; Feinstein, D.; Zanotti, S.; Taiberg, L.; Gurka, D. Duration of hypotension before initiation of effective antimicrobial therapy is the critical determinant of survival in human septic shock. *Crit. Care Med.* **2006**, *34* (6), 1589-1596.

2. Reinhart, K.; Bauer, M.; Riedemann, N. C.; Hartog, C. S. New approaches to sepsis: molecular diagnostics and biomarkers. *Clin. Microbiol. Rev.* **2012**, *25* (4), 609-634.

View Article Online
DOI: 10.1039/D6TB00732E

3. Moschou, D.; Tserepi, A. The lab-on-PCB approach: tackling the μTAS commercial upscaling bottleneck. *Lab Chip* **2017**, *17* (8), 1388-1405.

4. Bouadma, L.; Luyt, C. E.; Tubach, F.; Cracco, C.; Alvarez, A.; Schwebel, C.; Schortgen, F.; Lasocki, S.; Veber, B.; Dehoux, M.; Bernard, M. Use of procalcitonin to reduce patients' exposure to antibiotics in intensive care units (PRORATA trial): a multicentre randomized controlled trial. *Lancet* **2010**, *375* (9713), 463-474.

5. Schuetz, P.; Birkhahn, R.; Sherwin, R.; Jones, A. E.; Singer, A.; Kline, J. A.; Runyon, M. S.; Self, W. H.; Courtney, D. M.; Nowak, R. M.; Gaieski, D. F. Serial procalcitonin predicts mortality in severe sepsis patients: results from the multicenter procalcitonin Monitoring Sepsis (MOSES) study. *Crit. Care Med.* **2017**, *45* (5), 781-789.

6. Volanakis, J. E. Human C-reactive protein: expression, structure, and function. *Mol. Immunol.* **2001**, *38* (2-3), 189-197.

7. Liu, Z.; Huang, S.; Yan, Y.; Pang, W.; Zhong, F.; Huang, Q.; Caddeo, F.; Zhang, M.; Jin, M.; Shui, L. Multiplex Signal Amplification for Ultrasensitive CRP Assay via Integrated Electrochemical Biosensor Array Using MOF-Derived Carbon Material and Aptamers. *Talanta*. **2024**, *272*, 125735.

8. Miguel-Bayarri, V.; Casanoves-Laparra, E. B.; Pallás-Beneyto, L.; Sancho-Chinesta, S.; Martín-Osorio, L. F.; Tormo-Calandín, C.; Bautista-Rentero, D. Prognostic value of the biomarkers procalcitonin, interleukin-6 and C-reactive protein in severe sepsis. *Med. Intensiva* **2012**, *36* (8), 556-562.

9. Franco, D. M.; Arevalo-Rodriguez, I.; Figuls, M. R.; Oleas, N. G. M.; Nuvials, X.; Zamora, J. Plasma interleukin-6 concentration for the diagnosis of sepsis in critically ill adults. *Cochrane Database Syst. Rev.* **2019**, (4), No. CD012933.

10. Russell, C.; Ward, A. C.; Vezza, V.; Hoskisson, P.; Alcorn, D.; Steenson, D. P.; Corrigan, D. K. Development of a needle-shaped microelectrode for electrochemical detection of the sepsis biomarker interleukin-6 (IL-6) in real time. *Biosens. Bioelectron.* **2019**, *126*, 806-814.

11. Molinero-Fernandez, A.; Moreno-Guzman, M.; Arruza, L.; López, M. Á.; Escarpa, A. Toward early diagnosis of late-onset sepsis in preterm neonates: dual magnetoimmunosensor for simultaneous procalcitonin and C-reactive protein determination in diagnosed clinical samples. *ACS Sens.* **2019**, *4* (8), 2117-2123.

12. Zupančič, U.; Jolly, P.; Estrela, P.; Moschou, D.; Ingber, D. E. Multiplexed detection of sepsis markers in whole blood using nanocomposite coated electrochemical sensors. *medRxiv* **2020**, 2020.11.

View Article Online
DOI: 10.1039/D6TB00732E

13. Timilsina, S. S.; Jolly, P.; Durr, N.; Yafia, M.; Ingber, D. E. Enabling multiplexed electrochemical detection of biomarkers with high sensitivity in complex biological samples. *Acc. Chem. Res.* **2021**, *54* (18), 3529-3539.

14. Shukla, S.; Joshi, N. N.; Kadian, S.; Sahoo, S. S.; Narayan, R. J. Mixed metal conductive MOFs constructed from Trypan blue linked metal nodes: characteristic features and electrochemical performance. *J. Mater. Chem. C* **2025**, *13* (8), 3886-3901.

15. Doan, H. V.; Hamzah, H. A.; Prabhakaran, P. K.; Petrillo, C.; Ting, V. P. Nano-Micro Lett. **2019**, *11*, 1-33.

16. Xie, Y.; Wan, J.; Yan, Z.; Wang, Y.; Xiao, T.; Hou, J.; Chen, H. *Chem. Eng. J.* **2022**, *429*, 132237.

17. Li, L.; Huang, Y.; Fan, Y. Low-cost irreversible blue diode laser transmission welding of poly(methyl methacrylate)-based microfluidics. *Appl. Phys. A* **2022**, *128* (12), 1098.

18. Butova, V. V.; Burachevskaya, O. A.; Ozhogin, I. V.; Borodkin, G. S.; Starikov, A. G.; Bordiga, S.; Damin, A.; Lillerud, K. P.; Soldatov, A. V. UiO-66 type MOFs with mixed-linkers—1,4-benzenedicarboxylate and 1,4-naphthalenedicarboxylate: Effect of the modulator and post-synthetic exchange. *Microporous Mesoporous Mater.* **2020**, *305*, 110324.

19. Maranescu, B.; Plesu, N.; Visa, A. Phosphonic acid vs phosphonate metal organic framework influence on mild steel corrosion protection. *Appl. Surf. Sci.* **2019**, *497*, 143734.

20. Mukherjee, N.; Basu, O.; Mukhopadhyay, S.; Jana, T. Grafting of poly(vinyl phosphonic acid) to MOF surfaces to achieve proton conducting hybrid materials. *ACS Appl. Polym. Mater.* **2024**, *6* (13), 7488-7499.

21. Ruankham, W.; Tantimongcolwat, T.; Phopin, K.; Bausells, J.; Hangouet, M.; Martin, M.; Zine, N.; Errachid, A. Split aptamers immobilized array microelectrodes for detection of chlorpyrifos pesticide using electrochemical impedance spectroscopy. *Sens. Actuators B Chem.* **2022**, *372*, 132614.

22. Oliveira, S.; Jones, B. V.; Estrela, P.; Rocha, P. R.; Reis, N. M. Real-time monitoring of chemisorption of antibodies onto self-assembled monolayers deposited on gold electrodes using electrochemical impedance spectroscopy. *Langmuir* **2025**, ASAP.

23. Irimes, M. B.; Pusta, A.; Tertis, M.; Tabirta, A.; Achim, E.; Suciu, M.; Leostean, C.; Pana, O.; Oprean, R. N.; Cristea, C. Specific detection of cortisol in biological fluids: a tailored electrochemical aptasensing approach. *ACS Sens.* **2025**, ASAP.

24. Goda, T.; Higashi, D.; Matsumoto, A.; Hoshi, T.; Sawaguchi, T.; Miyahara, Y. Dual aptamer-immobilized surfaces for improved affinity through multiple target binding in potentiometric thrombin biosensing. *Biosens. Bioelectron.* **2015**, *73*, 174-180.

View Article Online
DOI: 10.1039/D6TB00732E

25. Whitehouse, W. L.; Lo, L. H.; Kinghorn, A. B.; Shiu, S. C.; Tanner, J. A. Structure-switching electrochemical aptasensor for rapid, reagentless, and single-step nanomolar detection of C-reactive protein. *ACS Appl. Bio Mater.* **2024**, *7* (6), 3721-3730.

26. Tseng, Y. T.; Yu, Y. H.; Yeh, Y. Y.; Mai, P. C.; Huang, T. T.; Huang, C. J.; Chau, L. K.; Chen, Y. L. Femtomolar-level detection of procalcitonin using a split aptamer-based fiber optic nanogold-linked sorbent assay for diagnosis of sepsis. *Talanta* **2023**, *293*, 128150.

View Article Online
DOI: 10.1039/D6TB00732E

Data Availability Statement

The methodologies and associated data are provided in the Supplementary Information file.